Modeling and experimental investigation of a controllable rotary fluid damper

X. CAO, J. ZHOU*), M. YU*), Y. WANG

College of Mechanical and Electrical Engineering,
Nanjing University of Aeronautics and Astronautics, Nanjing, 210016, China
e-mails*): *zhj@nuaa.edu.cn, yumin@nuaa.edu.cn (corresponding authors)*

CONTROLLABLE ROTARY FLUID DAMPER (CRFD) is an efficient and cheap energy dissipation device, which is used to reduce the impact of vibration in mechanical systems. In this paper, the CRFD controlled by a servo motor is developed to reduce the effects of vibrations in the helicopter flight control system. The dynamic mechanical characteristic of the CRFD is experimentally investigated by the MTS machine. Due to the complex factors such as high shear thinning rate and compressibility of the damping medium, inertia of moving parts and internal friction, the CRFD studied has highly nonlinear hysteresis characteristics. The accuracy of the damper modeling is of great significance for designing effective vibration reduction methods. Therefore, a new generalized viscous–nonlinear elastic model is proposed to track the mechanical characteristics of CRFD. On the basis of parameter sensitivity analysis, the proposed generalized viscous–nonlinear elastic model is modified. According to the identification results of the modified model, the main parameters are fitted as polynomial functions of motor rotation angle. Through error analysis between analytical torques and experimental torques, it is concluded that the modified generalized viscous–nonlinear elastic model has the smallest error compared with Kwok and Maxwell models, which indicates that the proposed modified model can accurately describe the mechanical characteristics of the CRFD under different working conditions.

Key words: controllable damper, rotary damper, parametric modeling, sensitivity analysis, damper design.

1. Introduction

OWING TO THE CHARACTERISTICS OF HIGH RELIABILITY and low power requirements, the controllable fluid dampers have broad application prospects in the field of structural vibration control [1, 2]. The damping force of the controllable fluid dampers can be quickly and effectively controlled by adjusting the damping gap through the electric signal [3]. The CRFD, as an important member of controllable fluid dampers, has the advantages of smaller space requirements, no exposed sealing surfaces, stepless damping adjustment, as well as high energy absorption efficiency. As a result, it can be used in helicopter control system [4],

tracked vehicle suspension damping system [5], prosthetic joint system [6] and other structural protection systems. The CRFD makes up for the shortcomings of narrow damping frequency band and a poor effect of traditional passive rotary fluid damper [7, 8].

At present, the primary reason restricting the promotion and application of CRFD in engineering is how to establish an accurate mechanical model. Compared with the controllable straight-tube fluid damper, the internal flow field of the CRFD is complicated, which brings great inconvenience to the mechanical modeling. The mechanical modeling of CRFD is of great significance for its application in structural vibration reduction [9, 10].

The mechanical modeling of fluid damper is mainly divided into a parametric model and non-parametric model [11–13]. The parameters of non-parametric models generally have no physical meaning, such as neuro-fuzzy [14, 15], neural networks [16, 17], Chebyshev polynomials [18] and so on. Although the non-parametric model can describe the behavior of the fluid damper, a large amount of experimental data is required to train the model, which leads to a highly complex modeling process [19].

By comparison, parametric models are the ideal ones for fluid dampers as their parameters have specific physical meanings [20, 21]. These models are usually considered to be a combination of a series of mechanical elements, such as viscous damping, the Coulomb friction, linear or nonlinear springs, inertial elements, etc. These mechanical elements are usually combined in series or parallel to describe the external mechanical characteristics of dampers. The parametric models applied to fluid dampers mainly include generalized viscous models [22], Kelvin models [23], Maxwell models [24], hyperbolic tangent models, Bouc–Wen models [25], etc. Different kinds of parametric models can describe the mechanical properties of different dampers. It is necessary to study a suitable model for parameters estimation to obtain high modeling accuracy.

So far, most of the established parametric models lack the inertial mass and Coulomb friction terms of the moving parts in the damper that are normally very important factors for parametric modeling. First of all, the damper is often subjected to high-acceleration vibrations such as shock and high-frequency excitation. When the moving parts of the damper have a relatively large inertial mass, the additional inertial force cannot be ignored under high-frequency vibration. Secondly, the movable parts in the damper cannot be completely lubricated, and there is a certain friction phenomenon [26]. The generalized viscous model is usually composed of nonlinear damping, inertia, spring elements and friction in parallel. This model is suitable for tracking the nonlinear hysteresis characteristics of CRFD [22, 27].

In order to obtain a high-precision parametric model of the CRFD, a generalized viscous–nonlinear elastic model which includes inertia element, friction

element, nonlinear damping element, nonlinear elastic element and hysteretic element is proposed to match the dynamic characteristics of the designed CRFD. The results show that the proposed model can accurately capture nonlinear and hysteretic behavior of the damper, in comparison with the Kwok model and the generalized Maxwell model.

The other sections of this article are organized as follows: In Section 2, the structure and experimental test of designed CRFD are introduced. In Section 3, a novel mechanical model for the CRFD is established. Section 4 presents the parameter sensitivity analysis and model simplification. Section 5 elaborates the parametric regression of the proposed model. Section 6 mainly describes the proposed model validation. Section 7 elaborates the error analysis of three models. Finally, the conclusions are given in Section 8.

2. Test damper and experimental measurements

2.1. The structure of designed CRFD

The vibration of helicopter flight control system mainly comes from the exciting force of main rotor, engine, reducer, etc. The forced vibrations of the main rotor and engine are the main exciting source of the helicopter flight control system, as shown in Fig. 1(a). The vibrations are transmitted to the joystick through the steering gear system, connecting rod, rocker arm and other parts. These causes discomfort of the driver's arm. In addition, excessive vibration will lead to deformation, friction and jamming of the connecting components in the helicopter flight control system, which may lead to helicopter losing control and even serious flight accidents.

A CRFD controlled by servo motor is developed which is mainly used to reduce the vibration response of helicopter flight control system, as shown in Fig. 1(b). The CRFD is composed of a rotor blade, a shell, two baffles, a regulating mechanism, a connecting arm, a servo motor, some bolts, etc. The basic parameters of the damper are shown in Table 1.

The working principle of the designed CRFD is as follows: When the main structure vibrates, the CRFD is driven to work through the link arm. If the rotor blade of damper rotate counterclockwise, the cavities A and D squeezed by the rotor blade become high-pressure zones, and the cavities B and C stretched by the rotor blade become low-pressure zones. The damping medium flows from the high-pressure cavities to the low-pressure cavities through the damping holes and damping channels. The directions of the damping medium flow are shown by the red arrows in Figs. 1(c) and 1(d). It should be noted that only the damping hole axes of cavities A and D are co-linear and the damping hole axes of cavities B, and C are co-linear. The damper drives the regulating mechanism through a servo
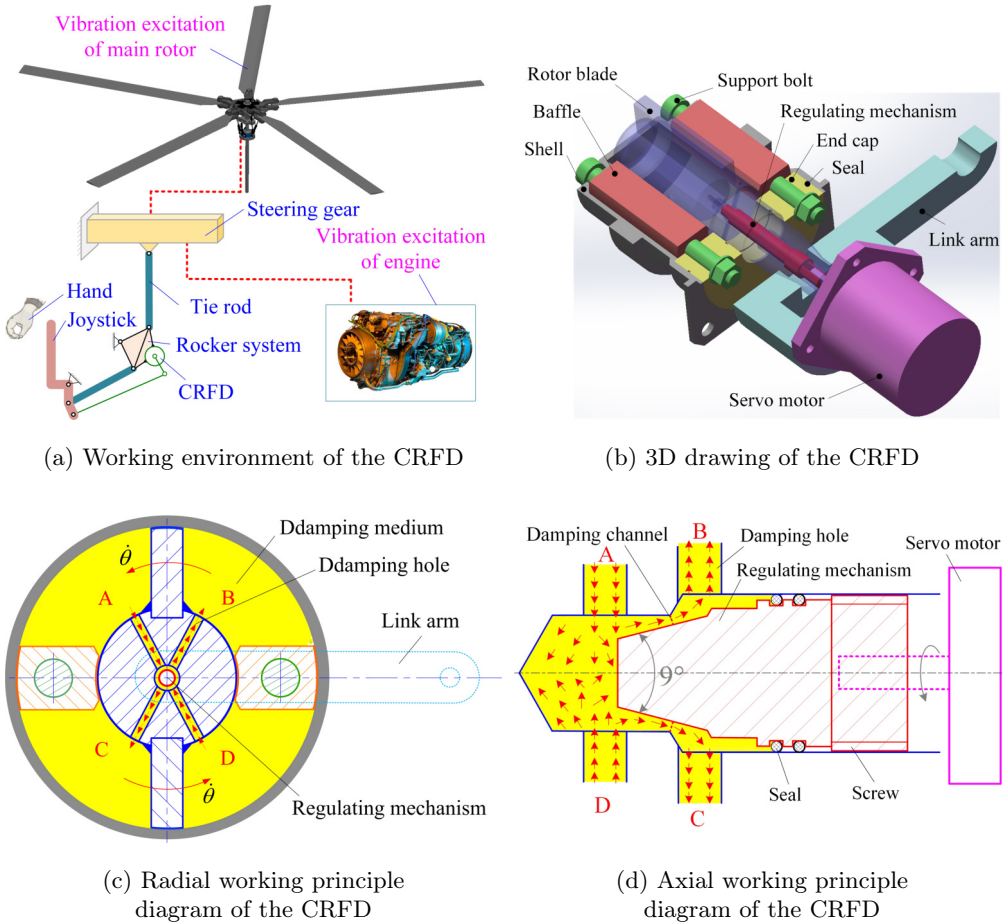
(a) Working environment of the CRFD

(b) 3D drawing of the CRFD

(c) Radial working principle
diagram of the CRFD

(d) Axial working principle
diagram of the CRFD

Fig. 1. Working environment and composition of the CRFD.

Table 1. Basic parameters of the experimental CRFD.

Parameters	Value
Rotor blade diameter [mm]	49
Rotor blade length [mm]	39
End taper of regulating mechanism [°]	9
Dynamic viscosity of damping medium [kg/(m·s)]	1.17×10^{-2}
Shell mass [kg]	0.28
Rotor blade mass [kg]	0.36
Servo motor mass [kg]	0.47
Damping medium mass [kg]	0.14

motor and a screw mechanism with a pitch of 1 mm to change the size of the damping channel, thereby adjusting the size of the damping torque. 180 degree is defined as the position where the regulating mechanism rotates to the bottom of the hole (that is, the position with the maximum damping torque). As the adjusting screw rotates counterclockwise outwards, the degree representing its position gradually increases and the corresponding damping torque gradually decreases; 0 degrees is designated as the position with the minimum damping torque.

2.2. Experimental testing

Experimental data of the CRFD was acquired under sine displacement excitation on an MTS testing machine. The MTS is made in the United States, whose force capacity is 5.5 kN. It has displacement and force sensors to collect the real-time displacement and the output damping force, respectively, as shown in Fig. 2(a). Set the measurement range of the force sensor to 1 kN. The sampling frequency of the MTS sensors is set manually according to the excitation conditions. For a low frequency and a small amplitude, set a lower sampling frequency. For a high frequency and large amplitude values, set a larger sampling frequency. The CRFD is connected to the collet of the MTS machine via a slider-crank mechanism. In order to avoid exceeding the maximum stroke of the CRFD, before each test, the link arm needs to be positioned in a horizontal position (i.e. the middle position of the CRFD working stroke).

The principle of the experimental device is shown in Fig. 2(b). The slider crank mechanism used is made of light aluminum alloy, so the inertia force of each component is not considered. The kinematic analysis of the slider-crank mechanism can be obtained as:

$$(2.1) \qquad \begin{cases} L_{AB} \cdot \cos\theta - L_{BC} \cdot \cos\gamma = 0, \\ L_{AB} \cdot \sin\theta + L_{BC} \cdot \sin\gamma - H - x_e = 0, \end{cases}$$

where H represents the vertical distance from point A to point C when the position of the link arm is in the horizontal position (i.e., when $\theta = 0$), here $H = 114.89$ mm. L_{AB} indicates the length of the link arm, $L_{AB} = 80$ mm. L_{BC} is the length of the link rod, $L_{BC} = 140$ mm, x_e denotes the real-time displacement collected by the displacement sensor MTS testing machine.

The torque T_0 produced by the load can be expressed as:

$$(2.2) \qquad T_0 = F_e \cdot \sin\gamma \cdot L_{AB} \cdot \sin(\theta + \gamma),$$

where F_e denotes the real-time force measured by the force sensor of MTS testing machine.
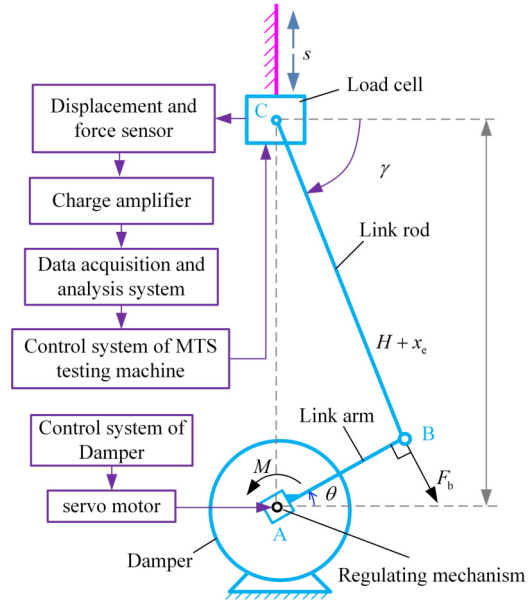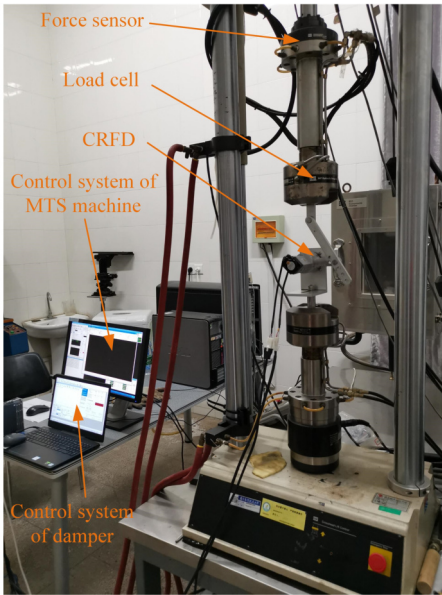
(a) Photograph of the test apparatus   (b) Schematic diagram of test apparatus

Fig. 2. Composition of the test apparatus.

By adjusting the angle of the servo motor, excitation amplitude and excitation frequency, the damping output torque of the CRFD can be obtained under different working conditions. The angle of the servo motor is selected as $0°$, $30°$, $60°$, $90°$, $120°$, $150°$ and $180°$. Six excitation amplitude levels, such as 0.8, 1, 1.5, 2, 2.5 and 3 mm (corresponding to the damper angular displacement amplitude of 0.01, 0.013, 0.019, 0.025, 0.031 and 0.037 rad), are considered in the testing, and the excitation frequencies are 1, 2, 3, 4 and 5 Hz. In order to obtain stable test data, each working condition should be repeated for 10 sinusoidal cycles.

2.3. Experimental results

Since the test data of the first three cycles and the last three cycles are unstable, the mechanical properties of the CRFD can be described by averaging the test data from the fourth to seventh cycles. The hysteresis curves of the CRFD with different servo motor angles, excitation amplitudes and frequencies are shown in Figs. 3–5.

Figure 3 shows the dynamic response of the CRFD output torque varying with the motor angle under the working condition of 3mm–2.5 Hz. It can be seen that with the increase of the motor angle, its damping torque gradually increases, and the corresponding energy dissipation also capacity increases gradually. This
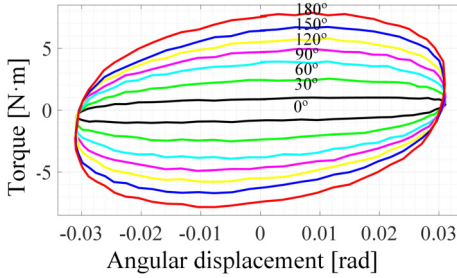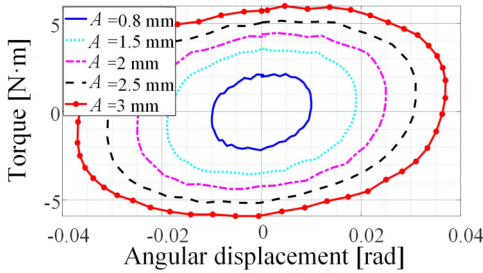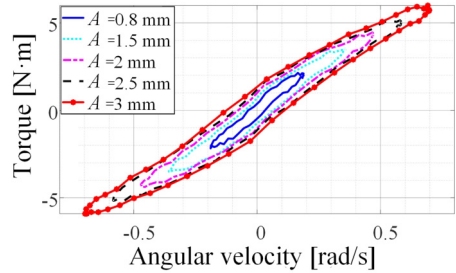
(a) Torque vs. angular displacement
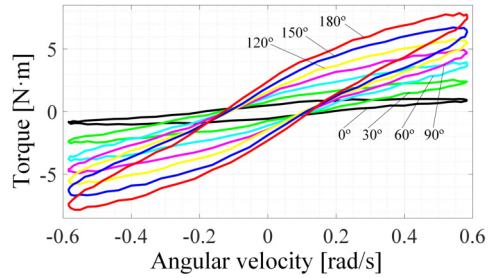
(b) Torque vs. angular velocity

Fig. 3. Damping torque varying with motor angle at 3 Hz–2.5 mm.
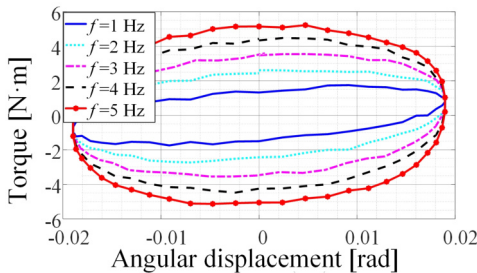

(a) Torque vs. angular displacement

(b) Torque vs. angular velocity

Fig. 4. Damping torque varying with excitation amplitude at 90°–3 Hz.

(a) Torque vs. angular displacement
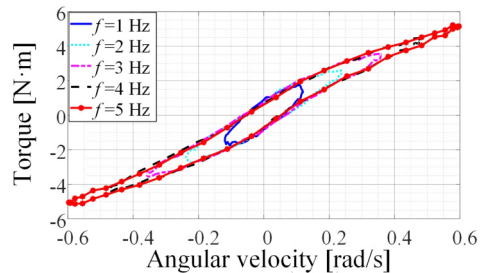
(b) Torque vs. angular velocity

Fig. 5. Damping torque varying with excitation frequency at 90°–1.5 mm.

is because the area of the damping gap decreases with the increase of the servo motor angle. When the angle of the motor reaches 180°, the damping torque of the motor will reach saturation due to the closing of the throttle gap at the rotating valve of the motor.

Figure 4 shows the dynamic response of the CRFD output torque to the excitation amplitude under the same working conditions (i.e. the same motor angle of 90° and the same excitation frequency of 3 Hz). It is obvious that with the increase of excitation amplitude, the maximum damping torque of CRFD output significantly increases, and the area enclosed by the damping torque–angular displacement loop also increases gradually (that is, the energy consumption of the damper gradually increases).

Figure 5 shows the dynamic response of the CRFD output torque to the excitation frequency under the same working conditions (i.e. the same motor angle of 90° and the same excitation amplitude of 1.5 mm). It can be concluded that with the increase of excitation frequency, the peak value of damping torque increases gradually, and the corresponding energy consumption also increases gradually.

The test curve of the CRFD has hysteresis characteristics and great nonlinearity, which is mainly because the output torque of damper is not only fluid viscous torque, but also consists of various kinds of torque. The output torque of the damper mainly includes viscous damping torque, elastic torque, Coulomb friction torque, inertia torque, etc. The viscous damping torque, which is the main form of damping torque, is produced by the viscous force of fluid. The elastic torque is caused by the compressibility of the gas in the damping medium. The Coulomb damping moment is generated due to the contact surface (including two pairs of annular surfaces and two pairs of parallel surfaces) between the CRFD rotor blades and the cylinder. Since the damper rotor, servo motor and other components occupy most of the inertia mass of the damper (as shown in Table 1), the inertia torque cannot be ignored during the movement.

3. Proposed model and initial verification

3.1. Proposed mechanical model

In order to accurately track the mechanical characteristics of CRFD, the next step is to model the various forms of torque that make up the damper output one by one.

To express the viscous damping effect of the CRFD, a nonlinear damping element with fractional section is introduced to describe the viscous damping effect of the damper. The viscous damping term T_C can be expressed as [26]

$$(3.1) \qquad\qquad T_C = c_r \, \mathrm{sgn}(\dot{\theta}) |\dot{\theta}|^{\alpha},$$

where c_r denotes the rotational viscous damping coefficient, $\dot{\theta}$ represents the rotational angular velocity of the CRFD, α denotes the angular velocity index of the damper, $\mathrm{sgn}(\cdot)$ represents the signum function.

In order to express the stiffness effect, a nonlinear elastic element with fractional sections is introduced to describe the stiffness effect of the CRFD. The stiffness term T_K can be obtained as shown below:

$$(3.2) \qquad T_K = k_r \operatorname{sgn}(\theta)|\theta|^\beta,$$

where k_r denotes the rotational stiffness damping coefficient, θ represents the rotational angular displacement of the CRFD rotor blade, β denotes the angular velocity index.

To express the friction effect between relative moving parts in the damper, the friction term T_F is as follows

$$(3.3) \qquad T_F = T_f \cdot \operatorname{sgn}(\dot{\theta}),$$

where T_f denotes the friction torque.

In order to express the inertia effect of the moving parts inside the damper, the inertia term T_J can be described as follows

$$(3.4) \qquad T_J = J\ddot{\theta},$$

where J represents the moment of inertia, $\ddot{\theta}$ is the rotational angular acceleration of the CRFD.

To describe the hysteretic characteristics of the damper on the damping torque –angular velocity curve, the hysteretic characteristics of the damping torque are tracked based on the modified hyperbolic tangent function. The hysteretic term T_H can be expressed as follows [28]:

$$(3.5) \qquad T_H = \eta \tanh\left[\tfrac{1}{2}(\mu\dot{\theta} + \xi\theta)\right],$$

where η determines the height of the hysteresis, μ and ξ are the coefficients which determine the hysteretic shape.

According to formulas (3.1)–(3.5), The proposed mechanical model (as shown in Fig. 6) for CRFD can be obtained as:

$$
\begin{aligned}
(3.6) \qquad T_0 &= T_J + T_C + T_K + T_F + T_H \\
&= J\ddot{\theta} + c_r \operatorname{sgn}(\dot{\theta})|\dot{\theta}|^\alpha + k_r \operatorname{sgn}(\theta)|\theta|^\beta \\
&\quad + T_f \operatorname{sgn}(\dot{\theta}) + \eta \tanh\left(\tfrac{1}{2}(\mu\dot{\theta} + \xi\theta)\right).
\end{aligned}
$$

The establishment of the model refers to the generalized viscous–linear elastic model in reference [22]. Therefore, the proposed novel mathematical model is called the generalized viscous–nonlinear elastic model (GV–NEM) here.
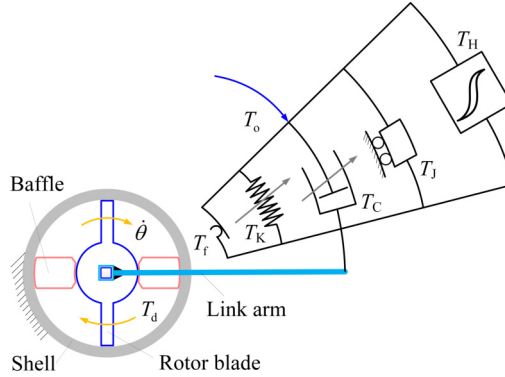
Fig. 6. Proposed model for CRFD.

3.2. Initial validation of GV-NEM effectiveness

In order to preliminarily explore whether the proposed GV–NEM can track the dynamic mechanical properties of CRFD, several experimental conditions are selected for parameter identification. An adaptive genetic algorithm is used in the recognition process. The detailed parameter identification process can refer to the previous papers of the authors [29, 30]. The 9 parameters to be identified in the proposed GV–NEM are as follows

$$(3.7) \qquad \Theta = [J, c_{\mathrm{r}}, k_{\mathrm{r}}, \alpha, \beta, \eta, \mu, \xi, T_{\mathrm{f}}].$$

The identification results of working conditions 1 Hz–1 mm and 3 Hz–3 mm are shown in Tables 2 and Table 3. By substituting the identified parameter values into the proposed GV–NEM, the damping torque calculation results of the model can be obtained. Figures 7 and 8 show the comparison between the experimental results and the GV–NEM simulation results. It can be seen that

Table 2. Model parameter identification results at 1 Hz–1 mm.

GV–NEM	J [kg · m^2]	c_{r} [Nm/(rad/s)]	α	k_{r} [Nm/(rad)]	β	T_{f} [Nm]	η	μ	ξ
0°	0.011	1.784	0.824	2.719	0.929	0.012	0.129	4.963	49.192
30°	0.012	4.185	0.886	3.048	0.827	0.028	0.202	6.566	48.944
60°	0.011	6.522	0.858	5.498	0.866	0.038	0.228	7.239	49.352
90°	0.011	7.321	0.925	8.360	0.87	0.047	0.592	7.678	46.105
120°	0.012	7.417	0.817	10.536	0.854	0.041	0.557	8.189	45.436
150°	0.010	9.459	0.867	12.634	0.914	0.017	0.692	8.883	47.964
180°	0.012	11.398	0.89	15.484	0.891	0.016	0.792	10.140	49.363

TABLE 3. Model parameter identification results at 3 Hz–3 mm.

GV–NEM	J [kg · m^2]	c_{r} [Nm/(rad/s)]	α	k_{r} [Nm/(rad)]	β	T_{f} [Nm]	η	μ	ξ
0°	0.011	0.277	0.852	12.268	0.907	0.015	0.419	6.865	48.551
30°	0.012	3.136	0.857	16.041	0.902	0.016	0.496	7.913	50.475
60°	0.011	4.668	0.863	23.772	0.901	0.018	0.494	7.278	50.243
90°	0.011	5.632	0.852	23.222	0.849	0.016	0.927	8.586	46.504
120°	0.012	7.045	0.868	28.176	0.89	0.025	0.843	8.764	46.724
150°	0.011	8.066	0.885	35.740	0.868	0.028	0.908	8.628	51.203
180°	0.012	9.991	0.892	42.049	0.865	0.019	1.173	11.012	52.941

the simulation results of the model are in good agreement with the experimental results, and the overall relative error is small. The results show that the proposed GV–NEM model can accurately trace the nonlinear and hysteretic characteristics of CRFD under various independent conditions.

Due to the large number of parameters (9 parameters in total) in the proposed GV–NEM for CRFD, it brings a big problem to the establishment of the
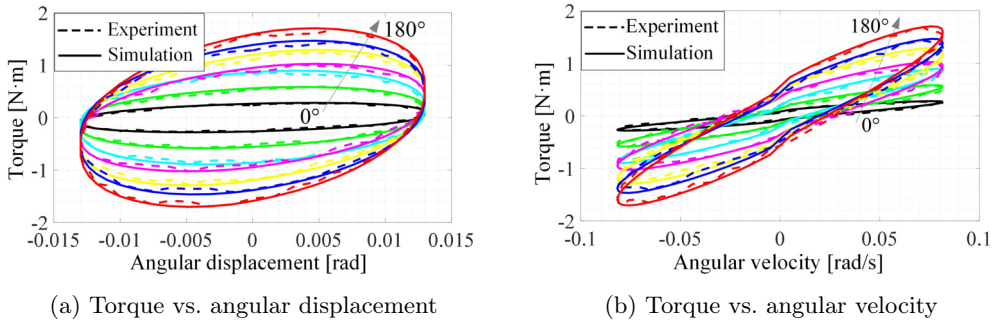

(a) Torque vs. angular displacement   (b) Torque vs. angular velocity

FIG. 7. Comparison between experiment and simulation at 1 Hz–1 mm.

(a) Torque vs. angular displacement   (b) Torque vs. angular velocity
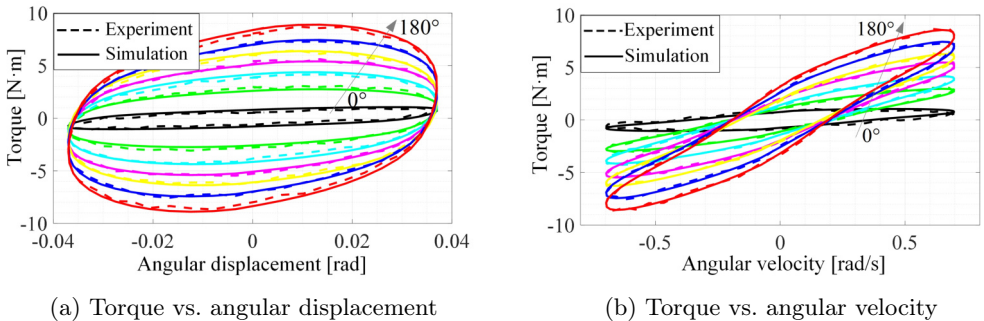
FIG. 8. Comparison between experiment and simulation at 3 Hz–3 mm.

normalized model (i.e., the model applicable to multiple working conditions). To simplify the proposed GV–NEM, the sensitivity of each parameter in the model to the output torque of CRFD is analyzed.

4. Sensitivity analysis and modification of GV–NEM

4.1. Parameter sensitivity analysis

Sensitivity analysis can quantitatively express the influence of input parameters on output. Generally speaking, parameters that have little influence on output can be found through sensitivity analysis, so as to simplify them.

TABLE 4. Values of $z_{i\,\min}$ and $z_{i\,\max}$ of each parameter in the model.

		J	c_r	α	k_r	β	T_f	η	μ	ξ
1 Hz–1 mm	$z_{i\,\min}$	0.006	3.661	0.463	4.180	0.435	0.024	0.296	3.839	23.053
	$z_{i\,\max}$	0.017	10.982	1.388	12.540	1.305	0.071	0.888	11.517	69.158
3 Hz–3 mm	$z_{i\,\min}$	0.006	2.816	0.426	11.611	0.425	0.008	0.464	4.293	23.252
	$z_{i\,\max}$	0.017	8.448	1.278	34.833	1.274	0.024	1.391	12.879	69.756

In order to analyze the contribution rate of each model parameter to the output torque, differential sensitivity analysis [31] is selected to calculate the sensitivity of each parameter, which can be expressed as follows

$$(4.1) \qquad S_{z_i} = \begin{cases} (f(z_i + \Delta z_i) - f(z_i))/\Delta z_i, & z_i = z_{i\,\min}, \\ (f(z_i + \Delta z_i) - f(z_i - \Delta z_i))/2\Delta z_i, & z_{i\,\min} < z_i < z_{i\,\max}, \\ (f(z_i) - f(z_i - \Delta z_i))/\Delta z_i, & z_i = z_{i\,\max}, \end{cases}$$

where $f(z)$ indicates the objective function of sensitivity analysis, z_i is the value of parameter z at the point i, and S_{z_i} denotes the sensitivity value of parameter z at the point i. Based on the 90° working condition, $z_{i\,\min}$ and $z_{i\,\max}$, are the values when the parameters change by negative 50% and positive 50%, respectively, as shown in Table 4. To represent the sensitivity in the interval $[z_{i\,\min}, z_{i\,\max}]$, the normalized S_z is given by

$$(4.2) \qquad S_z = \sqrt{\frac{1}{N} \sum_{i=1}^{N} S_{z_i}^2},$$

where S_z denotes the sensitivity of parameter z in the interval $[z_{i\,\min}, z_{i\,\max}]$, N is the total number of sampling points of parameter z data. To facilitate the comparative analysis of results, the percentage of sensitivity of each model parameter SP_{zj} can be obtained as [32]

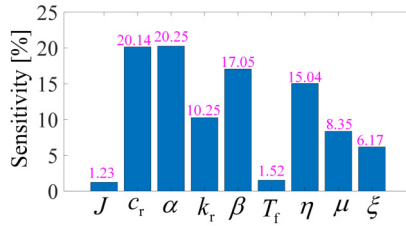$$(4.3) \qquad SP_{zj} = \frac{S_{zj}}{\sum_{j=1}^{n} S_{zj}} \times 100\%,$$

Fig. 9. Sensitivity analysis of model parameters.

where S_{zj} represents the sensitivity of the jth parameter, n indicates the total number of parameters.

Based on the above differential sensitivity analysis method, the sensitivity percentage of each parameter in the proposed GV–NEM can be obtained by averaging the analysis results under the conditions of 1 Hz–1 mm and 3 Hz–3 mm, as shown in Fig. 9. It can be seen that the sensitivity percentages of parameters c_{r}, α, β, η, k_{r}, μ is high, accounting for 20.14%, 20.45%, 17.04%, 15.04%, 10.25% and 8.35%, respectively, which account for a relatively large proportion. This indicates that these parameters are the main parameters of the model output. The sensitivity percentages of parameters J, T_{f} and ξ are 1.23%, 1.52% and 6.17%, respectively, which are relatively low, indicating that these parameters have influence on the output of the model.

4.2. Modified GV–NEM

As the change of parameters J, T_{f} and ξ have little influence on the output accuracy of the model, the identified data J, T_{f} and ξ are averaged under the working conditions of 1 mm–1 Hz and 3 mm–3 Hz. Although the sensitivity percentage of α and β is relatively large, the actual identification results mainly vary between 0.8–0.93, with a small range of variation. Therefore, the identified data α and β under the working conditions of 1 mm–1 Hz and 3 mm–3 Hz are also averaged. The proposed modified GV–NEM can be expressed as:

$$(4.4) \qquad T_0 = 0.011 \cdot \ddot{\theta} + c_{\mathrm{r}} \operatorname{sgn}(\dot{\theta})|\dot{\theta}|^{0.867} + k_{\mathrm{r}} \operatorname{sgn}(\theta)|\theta|^{0.880}$$
$$+ 0.024 \cdot \operatorname{sgn}(\dot{\theta}) + \eta \tanh\big(\tfrac{1}{2}(\mu\dot{\theta} + 48.786 \cdot \theta)\big).$$

There are only four parameters $(c_{\mathrm{r}}, k_r, \eta, \mu)$ to be identified in the improved model, which greatly improves identification efficiency. The improved model was identified under various test conditions (3 Hz–1 mm, 2 Hz–1 mm, 1 Hz–1 mm, 3 Hz–1.5 mm, 2 Hz–1.5 mm, 1 Hz–1.5 mm, 3 Hz–2.5 mm, 2 Hz–2.5 mm, 1 Hz–2.5 mm, 3 Hz–3 mm, 2 Hz–3 mm, 1 Hz–3 mm). The identification results are shown in Fig. 10.
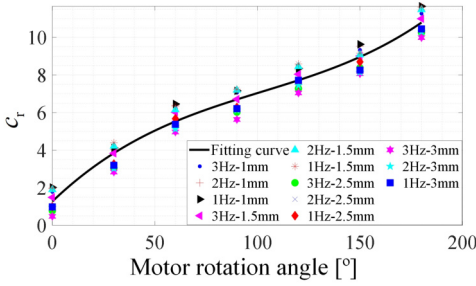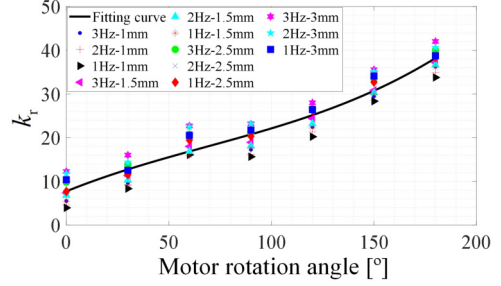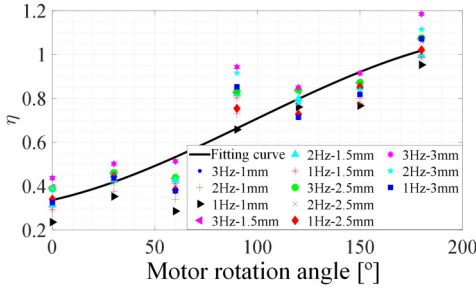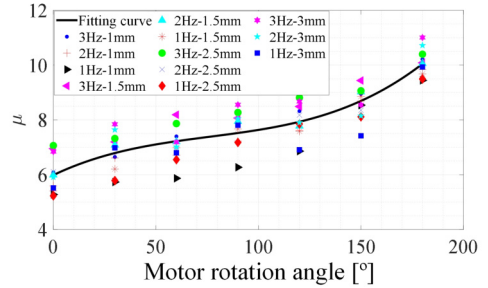
(a) Regression model curve of parameter c_r

(b) Regression model curve of parameter k_r

(c) Regression model curve of parameter η

(d) Regression model curve of parameter μ

Fig. 10. Regression model curve of parameters.

5. Regression of model parameters

In order to enable the model to track the dynamic mechanical characteristics under various working conditions, a regression model is established for the identified parameter values by using the curve fitting tool of MATLAB. The expression of cubic function fitting for parameters c_r, k_r, η, μ are as follows:

(5.1)
$$\begin{cases} c_r = c_{r3}\phi^3 + c_{r2}\phi^2 + c_{r1}\phi + c_{r0}, \\ k_r = k_{r3}\phi^3 + k_{r2}\phi^2 + k_{r1}\phi + k_{r0}, \\ \eta = \eta_3\phi^3 + \eta_2\phi^2 + \eta_1\phi + \eta_0, \\ \mu = \mu_3\phi^3 + \mu_2\phi^2 + \mu_1\phi + \mu_0. \end{cases}$$

The value of each parameter is shown in Table 5, and the fitting curve of parameters is shown in Fig. 10. It can be seen that the fitting curve can better track the change trend of each parameter. With the increase of motor angle ϕ, the value of parameters c_r, k_r, η, μ gradually increases.

TABLE 5. Values of regression model parameters.

Parameter	Value	Parameter	Value	Parameter	Value
c_{r0}	1.270	k_{r0}	7.739	η_0	0.337
c_{r1}	0.104	k_{r1}	0.190	η_1	2.065×10^{-3}
c_{r2}	-6.937×10^{-4}	k_{r2}	-8.880×10^{-4}	η_2	2.529×10^{-5}
c_{r3}	2.264×10^{-6}	k_{r3}	4.305×10^{-6}	η_3	-8.745×10^{-8}
μ_0	5.987	μ_1	3.568×10^{-2}	μ_2	-3.408×10^{-4}
μ_3	1.488×10^{-6}	J	0.011	α	0.867
β	0.880	T_f	0.024	ξ	48.786

6. Validation of the modified GV–NEM

In order to verify the effectiveness and adaptability of the proposed modified GV–NEM, experimental data under different working conditions (i.e. different frequencies and amplitudes, such as 2 Hz–1.5 mm, 3 Hz–2.5 mm and 4 Hz–1 mm) are used to verify the established regression model, as shown in Figs. 11–13.

(a) Torque vs. angular displacement   (b) Torque vs. angular velocity
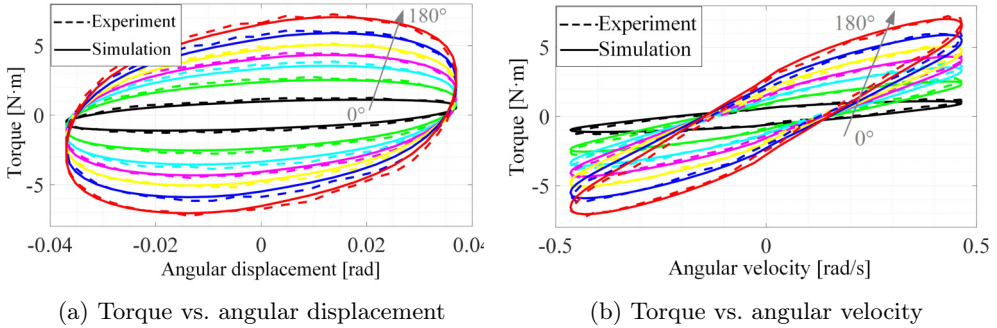
FIG. 11. Comparison between experiment and simulation at 2 Hz–3 mm.

(a) Torque vs. angular displacement   (b) Torque vs. angular velocity
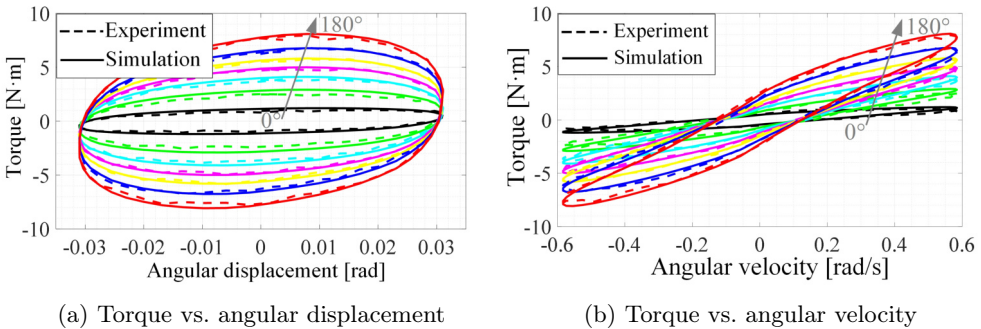
FIG. 12. Comparison between experiment and simulation at 3 Hz–2.5 mm.

(a) Torque vs. angular displacement
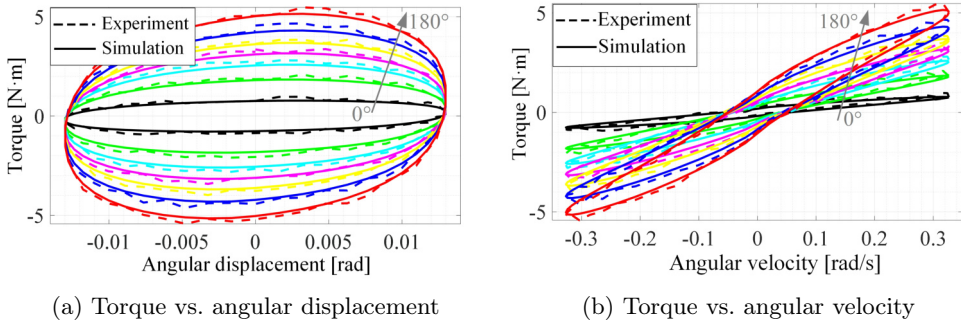
(b) Torque vs. angular velocity

Fig. 13. Comparison between experiment and simulation at 4 Hz–1 mm.

It can be seen from the figures that the damping torque–angular displacement and damping torque–angular velocity curves obtained through model simulation are in good agreement with the test curves. This indicates that the modified GV–NEM proposed in this research can track the nonlinear and hysteresis characteristics of CRFD well, and has high fitting accuracy.

7. Comparison of fitting effects by various models

To further verify the superiority of the proposed modified GV–NEM model, the Kwok model and the generalized Maxwell model, which are commonly used for fluid damper modeling, are selected for comparative analysis of fitting accuracy and error.

7.1. Kwok model

The Kwok model (as shown in Fig. 14) is mainly composed of damping element, stiffness element, bias force element and hysteresis element in parallel [26]. The model does not contain complex differential equations, and is widely used in
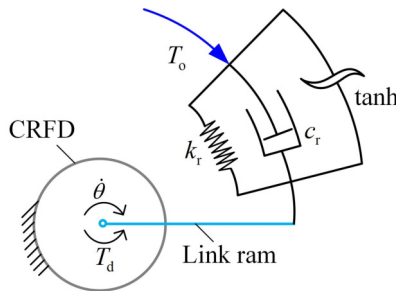

Fig. 14. Kwok model.

the parametric modeling of magnetorheological and fluid dampers. The equation of the Kwok model is given by:

$$(7.1) \qquad T_0 = c_\mathrm{r}\dot{\theta} + k_\mathrm{r}\theta + \eta\tanh(\mu(\dot{\theta} + \xi\operatorname{sgn}(\theta))) + T_\mathrm{r},$$

where θ indicates the rotational angular displacement of the CRFD; $\dot{\theta}$ is the rotational angular velocity of the CRFD; c_r denotes the rotational viscous damping coefficicient; k_r is the rotational stiffness coefficient; T_r represents the offset torque of CRFD; η is the main parameter affecting the magnitude of hysteresis torque; μ and δ are the parameters to determine the hysteresis shape of the hysteresis curve; $\operatorname{sgn}(\cdot)$ denote the signum function.

The parameters in the Kwok model are estimated using the test data of CRFD under different motor angle conditions. Six parameters that need to be identified in the model include c_r, k_r, η, μ, ξ and T_r. The identification method adopts the DE algorithm mentioned above. The parameters in the model are expressed as polynomial functions of the motor rotation angle, and the formula can be expressed as follows:

$$(7.2) \qquad \begin{cases} c_\mathrm{r} = c_\mathrm{r3}\phi^3 + c_\mathrm{r2}\phi^2 + c_\mathrm{r1}\phi + c_\mathrm{r0}, \\ k_\mathrm{r} = k_\mathrm{r3}\phi^3 + k_\mathrm{r2}\phi^2 + k_\mathrm{r1}\phi + k_\mathrm{r0}, \\ \eta = \eta_3\phi^3 + \eta_2\phi^2 + \eta_1\phi + \eta_0, \\ \mu = \mu_3\phi^3 + \mu_2\phi^2 + \mu_1\phi + \mu_0, \\ \xi = \xi_3\phi^3 + \xi_2\phi^2 + \xi_1\phi + \xi_0, \end{cases}$$

where the values of each parameter are shown in Table 6.

Table 6. Regression parameter values of Kwok model.

Parameter	Value	Parameter	Value	Parameter	Value
c_r0	0.915	k_r0	10.670	η_0	0.362
c_r1	0.071	k_r1	0.234	η_1	0.013
c_r2	-3.581×10^{-5}	k_r2	1.192×10^{-5}	η_2	-1.688×10^{-4}
c_r3	-2.407×10^{-7}	k_r3	1.644×10^{-6}	η_3	4.702×10^{-7}
μ_0	5.083	μ_1	0.315	μ_2	-6.399×10^{-3}
μ_3	2.880×10^{-5}	ξ_0	9.784	ξ_1	-31.540
ξ_2	9.919	ξ_3	-0.334	T_r	0.011

7.2. Generalized Maxwell model

In order to remedy the disadvantage that the traditional Maxwell model is only suitable for fluid dampers with relatively small amplitude or low frequency,

scholars put forward a generalized Maxwell model [33], as shown in Fig. 15. The generalized Maxwell model is mainly composed of nonlinear spring elements and nonlinear damping elements in series. The spring element and damping element in the model contain exponential coefficients. By adjusting the exponential coefficients, the generalized Maxwell model can simulate the complex viscoelastic behavior of the fluid damper. The formula of the generalized Maxwell model can be expressed as

$$(7.3) \qquad T_0 = c_{\mathrm{r}} \operatorname{sgn}(\dot{\theta}_{\mathrm{c}})|\dot{\theta}_{\mathrm{c}}|^{\alpha} = k_{\mathrm{r}} \operatorname{sgn}(\theta_{\mathrm{k}})|\theta_{\mathrm{k}}|^{\beta},$$

where c_{r} denotes the rotational viscous damping coefficient; $\dot{\theta}_{\mathrm{c}}$ indicates the rotational angular velocity of the viscous damping element; k_{r} represents the rotational stiffness coefficient; θ_{k} is the rotational angular displacement of the spring element; α indicates the angular velocity index of the viscous damping element; β denotes the angular displacement index of the spring element. The parameters θ_{k} and $\dot{\theta}_{\mathrm{c}}$ in the model need to meet the following kinematic conditions:

$$(7.4) \qquad \begin{cases} \theta = \theta_{\mathrm{c}} + \theta_{\mathrm{k}}, \dot{\theta} = \dot{\theta}_{\mathrm{c}} + \dot{\theta}_{\mathrm{k}}, \end{cases}$$

where θ is the angular displacement of CRFD; $\dot{\theta}$ is the angular velocity of CRFD; θ_{c} indicates the rotational angular displacement of the viscous damping element; θ_{k} is the rotational angular velocity of the spring element.
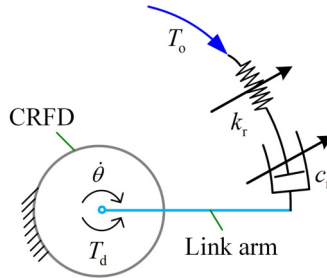

Fig. 15. Generalized Maxwell model.

The parameters in the generalized Maxwell model are estimated by using the damper test data under different motor angle conditions. The parameters that need to be identified in the model include c_{r}, k_{r}, α and β. The identification method also uses the DE algorithm mentioned above. The parameters in the model are described as polynomial functions of motor rotation angle, and the formula is as follows:

$$(7.5) \quad \begin{cases} c_{\mathrm{r}} = c_{\mathrm{r}3}\phi^3 + c_{\mathrm{r}2}\phi^2 + c_{\mathrm{r}1}\phi + c_{\mathrm{r}0}, \\ k_{\mathrm{r}} = k_{\mathrm{r}3}\phi^3 + k_{\mathrm{r}2}\phi^2 + k_{\mathrm{r}1}\phi + k_{\mathrm{r}0}, \\ \alpha = \alpha_3\phi^3 + \alpha_2\phi^2 + \alpha_1\phi + \alpha_0, \\ \beta = \beta_3\phi^3 + \beta_2\phi^2 + \beta_1\phi + \beta_0, \end{cases}$$

where the values of each parameter are shown in Table 7.

TABLE 7. Regression parameter values of generalized Maxwell model.

Parameter	Value	Parameter	Value	Parameter	Value
$c_{\mathrm{r}0}$	2.184	$k_{\mathrm{r}0}$	53.24	α_0	0.843
$c_{\mathrm{r}1}$	0.103	$k_{\mathrm{r}1}$	-0.367	α_1	1.288×10^{-4}
$c_{\mathrm{r}2}$	-1.938×10^{-4}	$k_{\mathrm{r}2}$	6.789×10^{-3}	α_2	1.688×10^{-5}
$c_{\mathrm{r}3}$	8.497×10^{-8}	$k_{\mathrm{r}3}$	-2.822×10^{-5}	α_3	-8.569×10^{-8}
β_0	0.943	β_1	-1.471×10^{-2}	β_2	1.546×10^{-4}
β_3	-5.089×10^{-7}				

7.3. Precision comparison

In order to compare the fitting accuracy of the three models, the curves simulated by the proposed modified GV–NEM, the Kwok model and the generalized Maxwell model are compared with the test curves.

The comparison of model reconstruction curve and test curve under different working conditions (60°–2 Hz–3 mm, 120°–3 Hz–2.5 mm, 180°–4 Hz–1 mm) are shown in Figs. 16–18 and Table 7. It can be seen that compared with the Maxwell model, the simulation results of the modified GV–NEM and the Kwok model are in good agreement with the test results, and the modified GV–NEM is in the best agreement. This shows that the modified GV–NEM and the Kwok
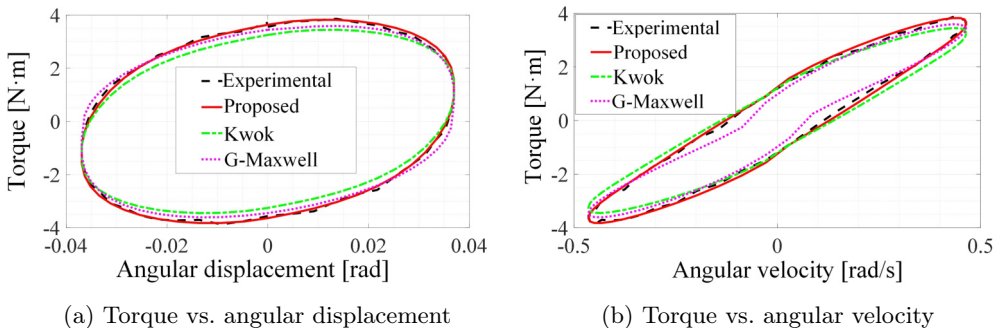

(a) Torque vs. angular displacement

(b) Torque vs. angular velocity

FIG. 16. Comparison between simulation and experiment of three models at 60°–2 Hz–3 mm.

(a) Torque vs. angular displacement   (b) Torque vs. angular velocity
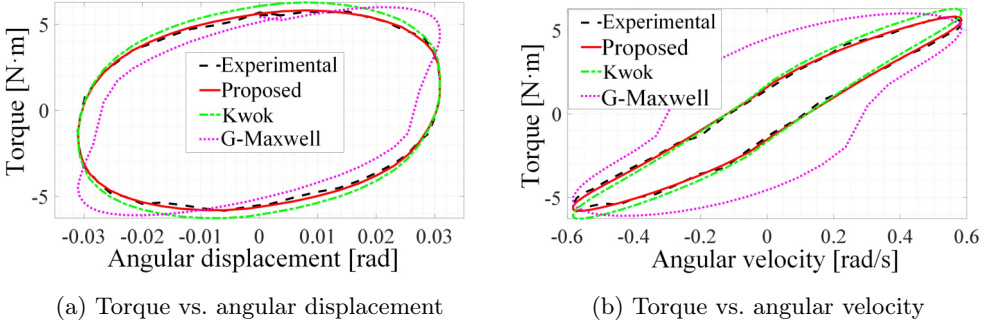
FIG. 17. Comparison between simulation and experiment of three models at
120°–3 Hz–2.5 mm.

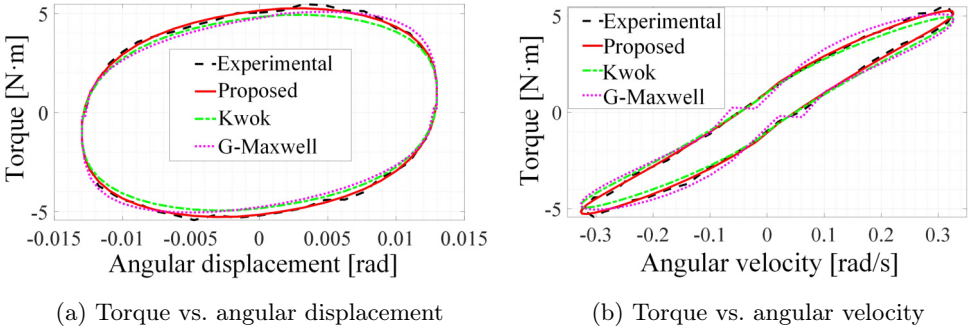(a) Torque vs. angular displacement   (b) Torque vs. angular velocity

FIG. 18. Comparison between simulation and experiment of three models at
180°–4 Hz–1 mm.

model can well capture the hysteresis characteristics of torque–angular velocity
and torque–angular displacement of CRFD, and the modified GV–NEM has the
best matching performance with the experimental data.

7.4. Error analysis

To further quantitatively analyze the fitting accuracy and verify the effectiveness of the improved model, the root mean square (RMS) errors between the simulated torque of the models and the experimental damping torque are used as the evaluation index of the accuracy of each model. The formula can be described as [25]

$$(7.6) \qquad \varepsilon = \sqrt{\frac{1}{2}\sum_{k=1}^{N}[T_e(t_k) - T_s(t_k)]^2}/T_{\max} \times 100\%,$$

where t_k denotes sampling time of the kth data; $T_e(t_k)$ represents the damping torque obtained from the test at t_k; $T_s(t_k)$ is the damping torque obtained from the model simulation at t_k time.

Table 8 shows the errors of the above three models under different motor angles and excitation conditions. The fitting error of the proposed modified GV–NEM is smaller than that of the Kwok model and the generalized Maxwell model under various condition. This indicates that the proposed modified GV–NEM in this paper has high accuracy and can be used as the parametric model of the designed CRFD.

Table 8. Error comparison of three models under different working conditions.

Excitation condition	Error (%)		
	Modified GV–NEM	Kwok model	Maxwell model
60○–2 Hz–3 mm	3.24	5.56	8.89
120°–2 Hz–3 mm	4.42	6.81	12.33
180°–2 Hz–3 mm	3.51	5.97	10.02
60°–3 Hz–2.5 mm	4.03	6.11	13.89
120°–3 Hz–2.5 mm	3.49	5.03	23.71
180°–3 Hz–2.5 mm	3.62	6.96	16.57
60°–4 Hz–1 mm	3.92	5.32	18.75
120°–4 Hz–1 mm	4.31	5.67	24.01
180°–4 Hz–1 mm	4.12	6.03	8.01

8. Conclusion

In this research, a CRFD controlled by a servo motor is developed to reduce the effects of vibrations in helicopter control systems. In order to analyze the dynamic mechanical characteristics of the damper, the mechanical experiments under different working conditions were carried out on the MTS testing machine. The accuracy of damper modeling is of great significance for designing effective vibration control strategies. Therefore, a new generalized viscous–nonlinear elastic model is proposed to track the mechanical characteristics of the CRFD. On the basis of parameter sensitivity analysis, the parameters of the proposed generalized viscoelastic nonlinear model are simplified. Through the error comparison between simulation and experiment, it is concluded that the error of the modified generalized viscous–nonlinear elastic model is the smallest compared with Kwok and generalized Maxwell models. Hence, the proposed modified model is suitable for the design of the controller and characterization of the dynamic mechanical behavior of the CRFD.

Conflict of interest

Funding

Acknowledgements

References

1. M.V. Waghmare, S.N. Madhekar, V.A. Matsagar, *Semi-active fluid viscous dampers for seismic mitigation of RC elevated liquid storage tanks*, International Journal of Structural Stability and Dynamics, **19**, 03, 1950020, 2019.

2. S. Bakhshinezhad, M. Mohebbi, *Multi-objective optimal design of semi-active fluid viscous dampers for nonlinear structures using NSGA-II*, Structures, **24**, 678–689, 2020.

3. M. Ahmadizadeh, *On equivalent passive structural control systems for semi-active control using viscous fluid dampers*, Structural Control and Health Monitoring, **14**, 6, 858–875, 2010.

4. Y.-J. Chen, *Development analysis of the inceptors for helicopter's fly-by-wire control system*, Helicopter Technique, **3**, 59–66, 2015.

5. C. Yang, X. Gao, Z. Liu, L. Cai, Q. Cheng, C. Zhang, *Modeling and analysis of the vibration characteristics of a new type of in-arm hydropneumatic suspension of a tracked vehicle*, Journal of Vibroengineering, **18**, 7, 4627–4646, 2016.

6. V.N.M. Arelekatti, N.T. Petelina, W.B. Johnson, A.G. Winter, *Design of a passive, shear-based rotary hydraulic damper for single-axis prosthetic knees*, ASME 2018 International Design Engineering Technical Conferences and Computers and Information in Engineering Conference, 2018.

7. R.S.T. Saini, S. Chandramohan, S. Sujatha, H. Kumar, *Design of bypass rotary vane magnetorheological damper for prosthetic knee application*, Journal of Intelligent Material Systems and Structures, **32**, 9, 931–942, 2021.

8. V.M. Arelekatti, N.T. Petelina, W.B. Johnson, A.G. Winter, M.J. Major, *Design of a passive, shear-based rotary hydraulic damper for single-axis prosthetic knees*, International Design Engineering Technical Conferences and Computers and Information in Engineering Conference, 51807, V05AT07A064, 2018.

9. F. Imaduddin, S.A. Mazlan, H. Zamzuri, *A design and modelling review of rotary magnetorheological damper*, Materials and Design, **51**, 575–591, 2013.

10. J.Q. ZHANG, Z.Z. FENG, Q. JING, *Optimization analysis of a new vane MRF damper*, Journal of Physics, Conference Series, **149**, 1, 012087, 2009.

11. R. MA, K. BI, H. HAO, *A novel rotational inertia damper for amplifying fluid resistance: Experiment and mechanical model*, Mechanical Systems and Signal Processing, **149**, 107313, 2021.

12. R. BOUC, *A mathematical model for hysteresis*, Acustica, **24**, 1, 16–25, 1971.

13. F. WEBER, G. FELTRIN, H. DISTL, *Detailed analysis and modelling of MR dampers at zero current*, Journal of Structural Engineering and Mechanics, **30**, 6, 787–790, 2008.

14. İ. ŞAHIN, T. ENGIN, Ş. ÇEŞMECI, *Comparison of some existing parametric models for magnetorheological fluid dampers*, Smart Materials and Structures, **19**, 3, 035012, 2010.

15. Y. HE, G. LIANG, B. XUE, Z. PENG, Y. WEI, *A unified MR damper model and its inverse characteristics investigation based on the neuro-fuzzy technique*, International Journal of Applied Electromagnetics and Mechanics, **61**, 2, 225–245, 2019.

16. C.C. CHANG, P. ROSCHKE, *Neural network modeling of a magnetorheological damper*, Journal of Intelligent Material Systems and Structures, **9**, 9, 755–764, 1998.

17. Y.A. YUCESAN, F.A. VIANA, L. MANIN, J. MAHFOUD, *Adjusting a torsional vibration damper model with physics-informed neural networks*, Mechanical Systems and Signal Processing, **154**, 107552, 2021.

18. R.C. EHRGOTT, S.F. MASRI, *Modeling the oscillatory dynamic behavior of electrorheological materials in shear*, Smart Materials and Structures, **1**, 4, 275, 1992.

19. K. HUDHA, H. JAMALUDDIN, P.M. SAMIN, R.A. RAHMAN, *Non-parametric linearised data driven modelling and force tracking control of a magnetorheological damper*, International Journal of Vehicle Design, **46**, 2, 250–269, 2008.

20. M. CHENG, Z. CHEN, W. LIU, Y. JIAO, *A novel parametric model for magnetorheological dampers considering excitation characteristics*, Smart Materials and Structures, **29**, 4, 045002, 2020.

21. W. WANG, Z. ZHOU, W. ZHANG, S. IWNICKI, *A new nonlinear displacement-dependent parametric model of a high-speed rail pantograph hydraulic damper*, Vehicle System Dynamics, **58**, 2, 272–289, 2020.

22. R. GRECO, J. AVAKIAN, G.C. MARANO, *A comparative study on parameter identification of fluid viscous dampers with different models*, Archive of Applied Mechanics, **84**, 8, 1117–1134, 2014.

23. A.R. GHAEMMAGHAMI, O.S. KWON, *Nonlinear modeling of MDOF structures equipped with viscoelastic dampers with strain, temperature and frequency-dependent properties*, Engineering Structures, **168**, 903–914, 2018.

24. W.O. WONG, C.N. WONG, *Optimal design of maxwell-viscous coulomb air damper with a modified fixed point theory*, Journal of Vibration and Acoustics, **143**, 3, 031002, 2021.

25. H. ZHU, X. RUI, F. YANG, W. ZHU, M. WEI, *An efficient parameters identification method of normalized Bouc–Wen model for MR damper*, Journal of Sound and Vibration, **448**, 146–158, 2019.

26. D.H. WANG, W.H. LIAO, *Magnetorheological fluid dampers: a review of parametric modelling*, Smart Materials and Structures, **20**, 2, 023001, 2011.

27. M.C. Constantinou, M.D. Symans, *Experimental study of seismic response of buildings with supplemental fluid dampers*, The Structural Design of Tall Buildings, **2**, 2, 93–132, 1993.

28. Y. Sun, Y. Huang, M. Wang, J. Wu, S. Yuan, J. Ding, Y. Peng, H. Pu, S. Xie, J. Luo, *Design, testing and modelling of a tuneable GER fluid damper under shear mode*, Smart Materials and Structures, **29**, 8, 085011, 2020.

29. X. Cao, M. Yu, J. Zhou, X. Guo, *Modeling and experimental verification of a semi-rotary fluid damper based on an improved Kelvin model*, Arabian Journal for Science and Engineering, **46**, 8, 7587–7596, 2021.

30. X. Guo, J. Zhou, X. Cao, Y. Wang, *Modeling and experimental study of a semi-active blade damper*, Engineering Mechanics, **39**, 10, 227–237, 2022.

31. D.M. Hamby, *A Review of Techniques for Parameter Sensitivity Analysis of Environmental Models*, Environmental Monitoring and Assessment, **32**, 2, 135–154, 1994.

32. M. Jiang, X. Rui, W. Zhu, F. Yang, H. Zhu, R. Jiang, *Parameter sensitivity analysis and optimum model of the magnetorheological damper's Bouc-Wen model*, Journal of Vibration and Control, **27**, 19–20, 2291–2302, 2021.

33. L.Y. Lu, G.L. Lin, M.H. Shih, *An experimental study on a generalized Maxwell model for nonlinear viscoelastic dampers used in seismic isolation*, Engineering Structures, **34**, 111–123, 2012.